ADVANCED MATERIALS INTERFACES

www.advmatinterfaces.de

Ultrathin Surface Coating Enables Stabilized Zinc Metal Anode

*Kangning Zhao, Chenxu Wang, Yanhao Yu, Mengyu Yan, Qiulong Wei, Pan He, Yifan Dong, Ziyi Zhang, Xudong Wang, and Liqiang Mai**

With the rapid development of energy storage devices, aqueous battery with noncombustion properties and instinct safe features has received great attentions and Zn anode is investigated intensively due to its high theoretical capacity (820 mAh g^{-1}), and low negative potential (–0.762 V vs SHE). However, the unavoidable gas evolution hinders the cyclability and the application in the commercial field. Herein, the atomic layer deposition of TiO_2 coating is first demonstrated as the protection layer of metallic zinc anode. The corrosion of zinc plate is significantly suppressed, leading to less gas evolution and $Zn(OH)_2$ byproduct formation. The reduced gas generation on the outer surface of the zinc plate will maintain the effective contact area between the electrolyte and anode and leads to an improved coulombic efficiency. In this way, the Zn anode with 100 ALD cycles TiO_2 protection shows reduced overpotential (72.5 mV) at 1 mA cm^{-2} for Zn–Zn symmetrical battery and additionally, the protection of TiO_2 extended the Zn–MnO_2 battery cycling performance up to 1000 cycles with the capacity retention of 85% at current density of 3 mA cm^{-2}. The novel design of atomic layer deposition protected metal zinc anode brings in new opportunities to the realization of the ultrasafe aqueous zinc metal batteries.

The present energy-storage landscape continues to be dominated by lithium-ion batteries.[1–7] However, growing concerns over the cost (lithium and cobalt), safety, environmental impact, and constrained resource supply drives researchers to search for alternative energy storage devices. Among those, aqueous batteries recently receive special interests by using the aqueous electrolyte which endows the advantages of nonflammability and the high ionic conductivity.[8–15] The intrinsic safe features and the excellent compatibility to atmosphere environment can free the aqueous batteries from complex battery management.[3,16,17] Therefore, aqueous electrolyte-based batteries can provide structural robustness and cost advantages over competing lithium-ion batteries. Among those aqueous batteries, zinc metal batteries with zinc as anode including zinc-air battery and Zn–MnO_2 battery has been investigated intensively due to its high theoretical capacity (820 mAh g^{-1}), low negative potential (–0.762 V vs SHE), abundance, low toxicity, and the intrinsic safety advantages.[18–30] In this regard, aqueous zinc ion batteries are expected to make substantial impacts toward advanced energy storage technologies, especially in stationary grid storage.

Despite the current success in exploration of cathode (including air cathode, MnO_2, and so on),[20,21,23,31–35] an important barrier of the Zn-based batteries is the poor cycle life, which mainly derives from the drawbacks of the Zn metal anode and the electrolyte. The zinc corrosion behavior in the alkaline electrolyte has been studied long time ago. Several successful strategies have been adopted to address the issue through the use of soluble additives in the alkaline electrolyte,[36] the redesign of zinc anode into three dimensional zinc foam[37] and so on. However, to date, there are few reports concerning the zinc anode protection in neutral or mild acidic aqueous electrolytes. Compared with the alkaline electrolyte where the charge carrier is $Zn(OH)_4^{2-}$

$$Zn(s) + 4OH^- \leftrightarrow Zn(OH)_4^{2-} + 2e^- \quad (1)$$

Zn metal is in contact with acidic electrolyte (pH value is ≈4) containing Zn^{2+} as the only soluble form and the charge carrier. In this way, Zn^{2+} ions act as charge carrier as follows

$$Zn(s) \leftrightarrow Zn^{2+} + 2e^- \quad (2)$$

Upon battery charging/discharging, Zn reversibly strips/plates on the anode and cathode repeatedly. Zn^{2+} prefers to deposit on Zn surface, leading to highly active Zn exposed in the slightly acidic electrolyte and facilitate the surface-dependent side reactions (e.g., corrosion, hydrogen evolution). This is especially severe when the pH value is decreased to below 4.[38] The hydrogen evolution occurring over time will leads to the electrolyte drying out, which result in a shortened battery life.[38] Meanwhile, accompanied with the hydrogen

K. N. Zhao, C. X. Wang, Dr. M. Y. Yan, Prof. Q. L. Wei, P. He, Y. F. Dong, Prof. L. Q. Mai
State Key Laboratory of Advanced Technology for Materials Synthesis and Processing
Wuhan University of Technology
Wuhan 430070, China
E-mail: mlq518@whut.edu.cn

K. N. Zhao, Dr. Y. H. Yu, Z. Y. Zhang, Prof. X. D. Wang
Department of Materials Science and Engineering
University of Wisconsin-Madison
Madison, WI 53705, USA

The ORCID identification number(s) for the author(s) of this article can be found under https://doi.org/10.1002/admi.201800848.

DOI: 10.1002/admi.201800848

generation, the hydration effects of the Zn(II) cation in water due to the loss of solvent will be accelerated and zinc hydroxide is easily forms.[39–41] Moreover, the gradual consumption of zinc anode will result in sub-optimal utilization of the zinc theoretical capacity.[40,42–47]

In order to explore the strategy addressing the problem mentioned above, the interface between zinc electrode and electrolyte is one of the most important issues of the battery. Among those, atomic layer deposition (ALD) is a unique technique that can realize excellent coverage and conformal deposition and the thickness of the film deposited by ALD can be precisely controllable at the nanoscale level due to its self-limiting nature.[48,49] Previous work has indicated that an ALD coating layer on the cathode and/or anode material for lithium/sodium battery prevents direct exposure of the electrolyte in the electrode, resulting in the formation of a stable electrolyte/electrode interphase, thereby increasing the electrochemical performance of the lithium/sodium batteries.[48,49] Thus, it is expected that the ALD coating strategy will improve the zinc anode performance.

Herein, we demonstrated the successful design of an ultrathin protective coating for zinc metal anode to achieve long life and high efficiency zinc metal batteries. The amorphous TiO_2 layer is chosen as the protective layer for its electrochemically and chemically stable in withstanding the harsh battery operation conditions according to the Pourbaix diagram among those commonly adopted materials (such as Al_2O_3, VO_x; Figure S1, Supporting Information). The highly electrical conductive and conformal TiO_2 layer acts as passivation layer between the electrode and the electrolyte, avoiding the direct contact between the zinc plate and the electrolyte and suppressing the gas evolution and the formation of less conductive $Zn(OH)_2$ (**Figure 1**). Thus, it can be anticipated that with the ultrathin TiO_2 coating, the performance of zinc anode can be significantly enhanced in mild acidic aqueous electrolytes and

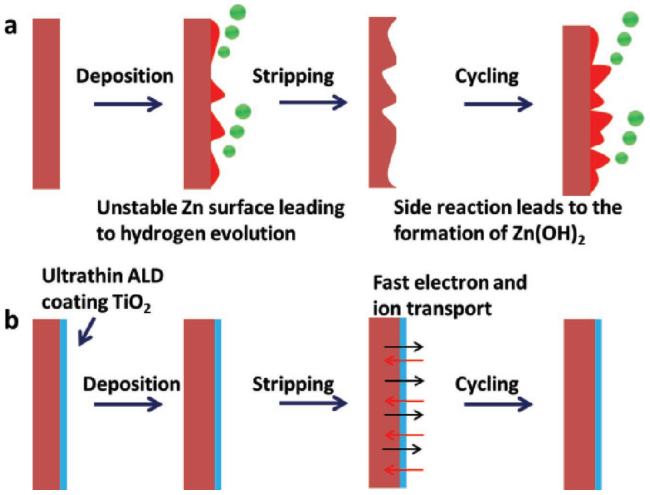

Figure 1. Schematic illustration of the stabilization of zinc anode with TiO_2 coating. a) Repeated plating/stripping cycles result in zinc corrosion and hydrogen evolution. The decomposition of the solvent in aqueous electrolyte will accelerate the Zn^{2+} dehydration, leading to the formation of less conductive $Zn(OH)_2$. b) A thin layer of TiO_2 coating leads to a stable cyclic deposition/stripping process, getting rid of the severe gas evolution and the formation of less conductive $Zn(OH)_2$.

further applied in the high energy density aqueous batteries with Zn as anode.

The ultrathin TiO_2 coating process via ALD process involves two precursors ($TiCl_4$ and H_2O run) in sequence with an extensive N_2 purge between the pulses of two precursors. Repeating full pulse/purge cycles for the alternating precursors allows atomically precise layer-by-layer growth of ultrathin film. The morphology is initially characterized by top view scanning electron microscope (SEM). For the pristine zinc plate, a rough and textile surface can be observed (Figure S2, Supporting Information). After 100 cycles ALD process, the product (denoted as $100TiO_2$@Zn) shows flakes-like shape in different size on the surface of the zinc plate in Figure S3 of the Supporting Information. In order to characterize the thickness of the layer, the cross-section image in TEM is carried out in **Figure 2**a and it is found that an amorphous layer is observed on the zinc plate with a thickness of 8 nm. The electron energy loss spectroscopic (EELS) mapping in Figure 2b reveals that the amorphous layer is composed of Ti and O, confirming that the surface layer is the as-deposited amorphous TiO_2 layer. The chemical state of the ultrathin coating TiO_2 layer is characterized by X-ray photoelectron spectroscopy (XPS) as XPS is a powerful tool to characterize the surface/near surface (≈ 5 nm) chemistry. Figure 2d shows that the Ti 2p spectrum in the surface is composed of only two peaks, 459.3 and 465.0 eV, corresponding to the characteristic peaks of Ti^{4+} 2p 1/2 and 2p 3/2 peak, respectively. XPS depth profiling in Figure S5 of the Supporting Information, by combining ion gun etch cycles interleaved with XPS measurements, was also used to provide the composition along the thickness of the coated electrode and depicts the intensity evolution for Zn, Ti, and O components in the coated electrode, as a function of the etching time. On the basis of the XPS depth-profile, the TiO_2 layer is further confirmed and after 70 min etching, the Ti peak gradually disappears, suggesting that the thickness TiO_2 layer is 8 nm, which is consensus to the observation in the cross-sectional STEM image in Figure 2a. Figure 2c shows the Ti 2p spectrum after 80 min etching. It is found that Ti^{3+} 2p 1/2 and 2p 3/2 peaks gradually appear, suggesting that the amorphous TiO_2 is composed of intermediate phase, such as Zn–O–Ti bonding formation.[50] As a contrast, the product after 500 cycles ALD process (denoted as $500TiO_2$@Zn) is also carried out. The top-view SEM images in Figure S4a of the Supporting Information show the flakes-like shape structure on the surface of zinc plate. Under higher magnification, some small particles are observed on the layer in Figure S4b of the Supporting Information, indicating the surface is saturated with TiO_2. The coating layer on the zinc plate is further subjected to XRD characterization (Figure 2e). All the samples show the characteristic peak of zinc metal (JCPDS No. 065-5973). The commercial zinc plate shows dominant peaks at 36.2° and 70.1°, which corresponds to plane (002) and (103) of Zn, respectively. Additionally, XRD patterns of $100TiO_2$@Zn plate and $500TiO_2$@Zn show decreased intensities in (100) and (110), which is believed to retard the hydrogen evolution and zinc corrosion during electrochemical reaction.[47] The zinc corrosion curves are tested in a mild acidic electrolyte (3 M $Zn(CF_3SO_3)_2$ solution; pH value is ≈4.0). The corrosion curves of pristine zinc plate, $100TiO_2$@ zinc plate, and $500TiO_2$@zinc plate is shown in Figure 2f. The

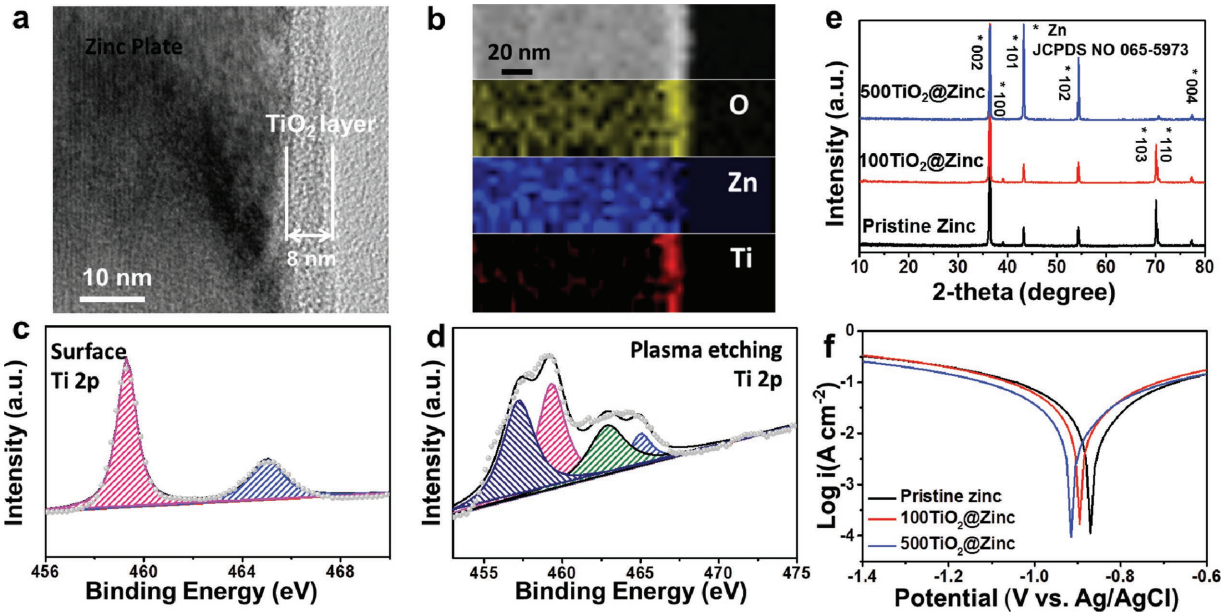

Figure 2. a) Cross-sectional STEM image and b) corresponding EELS mapping of 100TiO_2@Zn. c,d) Ti 2p XPS spectrum of 100TiO_2@Zn in the surface and after etching. e) XRD patterns of pristine zinc, 100TiO_2@Zn, and 500TiO_2@Zn. f) Corrosion curves of pristine Zn, 100TiO_2@Zn, and 500TiO_2@Zn in 3 M $Zn(SO_3CF_3)_2$ electrolyte.

exchange currents of pristine zinc plate, 100TiO_2@zinc plate are similar while that of 500TiO_2@zinc plate decreases with the increasing ALD cycles of TiO_2. The overpotential of pristine zinc is the highest among the three samples (–0.87 V vs Ag/AgCl). The overpotential of 100TiO_2@Zn decreases to –0.89 V while 500TiO_2@Zn to the lowest value (–0.91 V). These results indicate that TiO_2 layer can act as corrosion inhibitor, which prevents the zinc anode from the zinc corrosion.

The electrochemical performance of the zinc plates with different TiO_2 coating thicknesses was studied in a symmetrical cell configuration using 3 M $Zn(SO_3CF_3)_2$ as electrolyte.[24,51] **Figure 3**a shows the cycling stability of the symmetrical cells at rate of 1 mA cm^{-2} and a limited capacity of 1 mAh cm^{-2}. The pristine zinc anode shows initial passivation process with high polarization in voltage (Figure S6b, Supporting Information), and become stabilized after 35 h. After stabilization, the pristine zinc anode shows small voltage hysteresis (Figure S6c, Supporting Information) and the overpotential is ≈72.5 mV after cycling for 95 h. However, the voltage hysteresis gradually increases and finally leads to the cell death (Figure S6d, Supporting Information). In comparison, 100TiO_2@Zn keeps stable for over 150 h without initial passivation process with a lower overpotential of ≈57.2 mV. 500TiO_2@Zn shows even lower voltage hysteresis (≈40.9 mV) in Figure S6a of the Supporting Information. However, after only 70 h, the voltage hysteresis increases and ultimately leads to the cell failure. The passivation process may be linked to better wettability between Zn plate and the electrolyte as shown in Figure S7 of the Supporting Information. The electrochemical impedance spectroscopy (EIS) of the Zn/Zn symmetrical cells is further evaluated in Figure S8 of the Supporting Information and 100TiO_2@Zn shows the lowest charge-transfer resistance, suggesting the optimized thickness of TiO_2 layer is ≈8 nm and it is believed that the 500-cycle TiO_2 film is too thick for zinc ions to transport through, which leads to the decreased performance. The surface morphology of zinc metal after 150 cycles was studied by ex situ SEM. Figure 3b and Figure S8b (Supporting Information) presents the top-view SEM images of bare zinc metal after repeated cycles for 150 h. Without TiO_2 coating, a large number of flakes are observed on the zinc plate. On the contrary, with 100 cycles TiO_2 protection, only few flakes are observed and the size is much smaller in Figure S8a of the Supporting Information, indicating the zinc corrosion is suppressed. The EDS spectrum of the region is given in Figure S9 of the Supporting Information, confirming the existence of TiO_2 on the surface. Ex situ XRD is further carried out in Figure 3d. After cycling, two new peaks at 12.4° and 24.9° appear, which correspond to the characteristic peak of $Zn(OH)_2$ (JCPDS No. 038-0356) in both pristine zinc and 100TiO_2@Zn. This suggests that the flakes observed in Figure 3b are $Zn(OH)_2$.[52,53] The peak intensities of pristine zinc are much higher than that of 100TiO_2@Zn, which also indicates that with TiO_2 coating, the formation of less conductive $Zn(OH)_2$ is greatly suppressed. To further characterize the surface state of zinc plate, the ex situ XPS depth-profile of 100TiO_2@Zn in Figure 3e shows two distinct layers covering the surface of the electrode. The upper layer consists $Zn(OH)_2$ layer on the surface as indicated by the intensity of Zn. The lower layer consists of the amorphous TiO_2 layer. In order to characterize the surface zinc layer, the detailed Zn 2p spectrum is shown in Figure 3f. A major peak at 1021.9 eV and only a small peak at 1023.1 eV are observed, corresponding to the Zn 2p1/2 spectrum of metallic Zn and $Zn(OH)_2$, respectively. On the contrary, the Zn 2p spectrum of pristine Zn plate without TiO_2 protection in Figure 3g shows only one peak at 1023.1 eV is observed, which is characterized to be the characteristic peak of $Zn(OH)_2$. Based on the result above, the surface layer (flakes) on the surface are confirmed to be $Zn(OH)_2$, rather than Zn dendrites, which is quite interesting, as it is thermodynamically

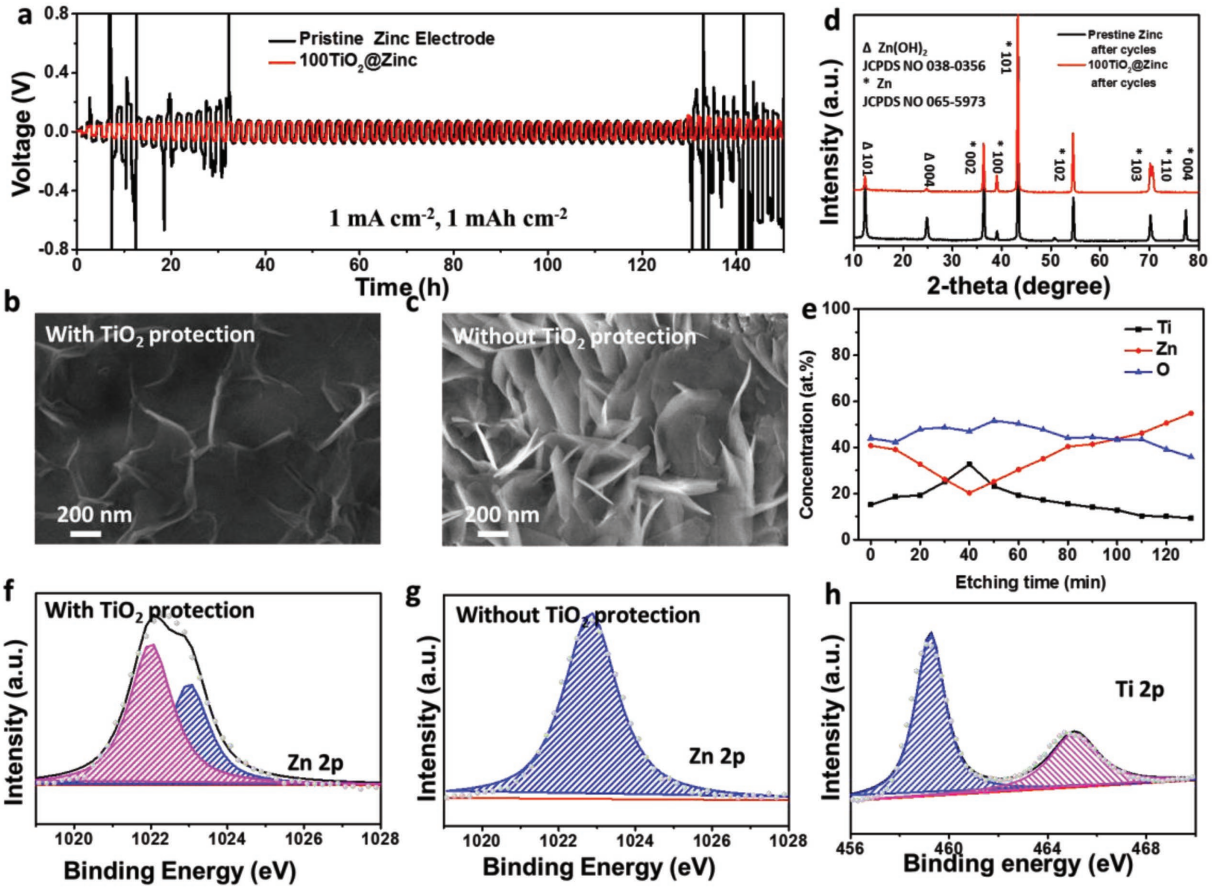

Figure 3. a) Cyclic deposition/stripping process of symmetric cells using $100TiO_2$@Zn and pristine Zn at a constant current density of 1 mA cm^{-2}. Each cycle is set to be 1 h. b,c) Ex situ SEM images of $100TiO_2$@Zn and pristine Zn anode, respectively. d) Ex situ XRD patterns of $100TiO_2$@Zn and pristine Zn anode. e) XPS depth profile of $100TiO_2$@Zn after cycling. f,g) Ex situ Zn 2p XPS spectrum of pristine Zn plate and $100TiO_2$@Zn, respectively. h) Ex situ Ti 2p XPS spectrum of $100TiO_2$@Zn.

unfavorable to form $Zn(OH)_2$ in the slightly acid solution. After long-term cycling, we noticed that there is electrolyte leakage in pristine Zn–Zn symmetrical cell, suggesting the possible gas emission in the battery. Thus, it is rational to suspect that formation of $Zn(OH)_2$ origins from the loss of solvent (water), leading to the hydrolysis of Zn^{2+}. Additionally, the Ti 2p spectrum of $100TiO_2$@Zn in Figure 3h is consisted of the characteristic peaks of Ti^{4+} 2p 1/2 and 2p 3/2 peak, which is the same as that in Figure 2d.

The zinc anode with TiO_2 protection is further applied in Zn–MnO_2 battery. α-MnO_2 nanowires are used as the cathode (Figure S10, Supporting Information). As shown in **Figure 4**a, the cell is initially cycled at 100 mA g^{-1} (corresponding to 0.65C for MnO_2 cathode and 0.3 mA cm^{-2} for zinc anode) and the charge–discharge curves at initial two cycles are shown in Figure S11a of the Supporting Information. With TiO_2 protection, $100TiO_2$@Zn-MnO_2 cell shows a reversible capacity of 235 mAh g^{-1} after 60 cycles and on the contrary, the Zn–MnO_2 cell shows rather a quick capacity fading and only 155 mAh g^{-1} is retained after 60 cycles. Moreover, the coulombic efficiency (CE) is also improved. After an initial activation process for 20 cycles, the $100TiO_2$@Zn–MnO_2 cell shows high CEs around 98.0% while the pristine Zn–MnO_2 cell shows rather lower CEs (≈96%) in Figure 4b. It is believed that the CE is highly related to the zinc corrosion and thus with higher CEs, the zinc corrosion is greatly prohibited. The $500TiO_2$@Zn is also tested as a comparison in Figure S11 of the Supporting Information and the $500TiO_2$@Zn–MnO_2 cell delivers rather lower reversible capacity of 209 mAh g^{-1} as well as the lowered CEs, compared with $100TiO_2$@Zn–MnO_2 cell. To further evaluate the zinc corrosion in the electrolyte, the self-discharge test was carried out by charging the cell to 1.8 V and resting in Figure 4c. It is found that after fully charged to 1.8 V, the voltages of both $100TiO_2$@Zn-MnO_2 cell and Zn–MnO_2 cell stabilize at 1.48 V after 2 h. However, after 370 h, the voltage of Zn–MnO_2 cell gradually drops and shows ups and downs trend while the voltage of $100TiO_2$@Zn-MnO_2 cell is stable for over 400 h. Additionally, it is also found that Zn–MnO_2 coin cell shows the leakage of electrolyte (inset of Figure 4c), while $100TiO_2$@Zn–MnO_2 cell remains stable without any electrolyte leakage. The leakage of electrolyte is believed to be related to the hydrogen evolution, which increase the internal pressure in the coin cell. The internal pressure gradually increases and at a certain point, the coin cell breaks, leading to the leakage of electrolyte. This phenomenon further confirms that with TiO_2 coating, the corrosion of zinc is largely prohibited and hydrogen evolution is

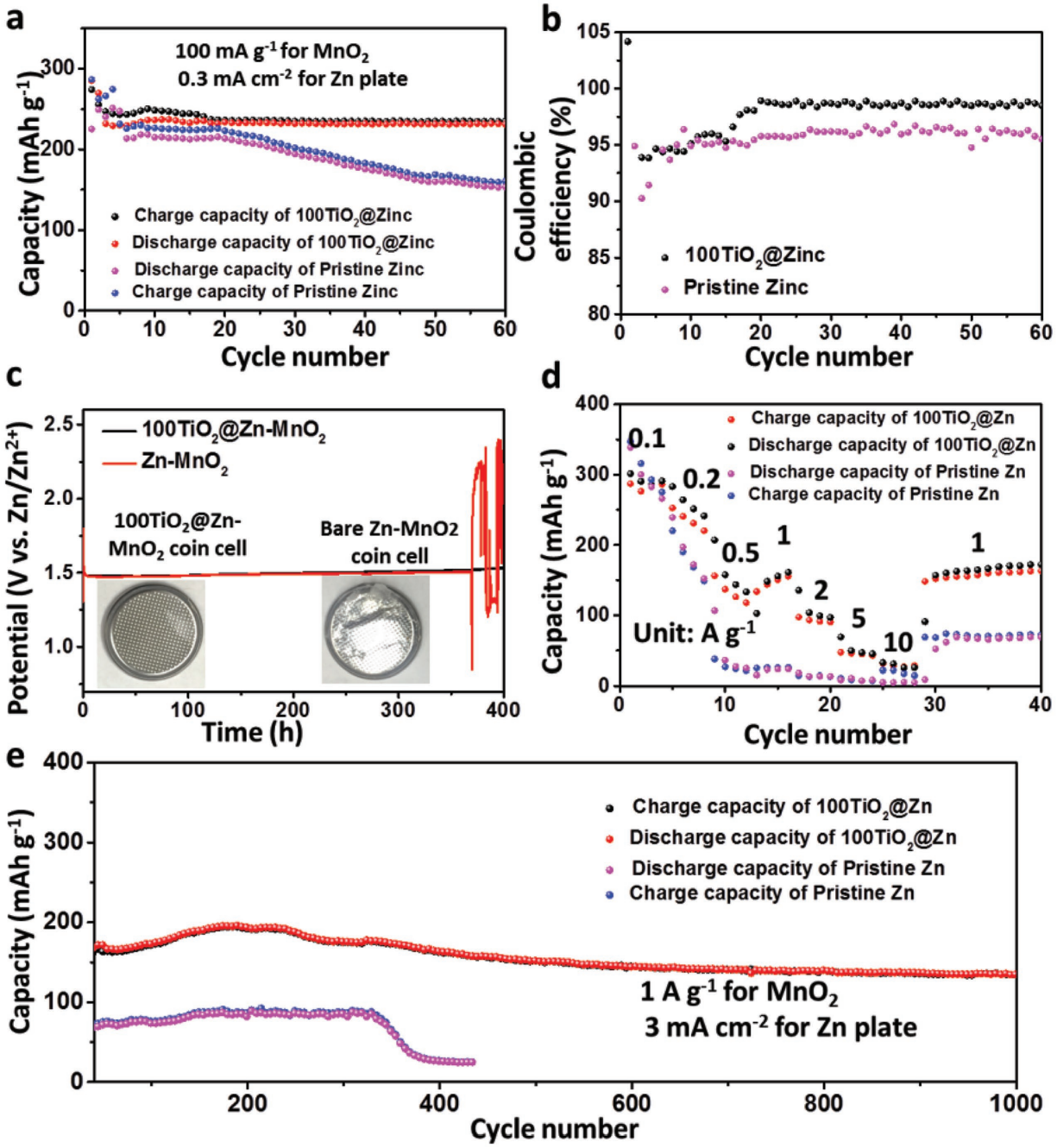

Figure 4. a) Cycling performance of $100TiO_2$@Zn–MnO_2 cell and Zn–MnO_2 cell at 100 mA g^{-1} (corresponding to 0.65C for MnO_2 and 0.4 mA cm^{-2} for zinc anode). b) Coulombic efficiencies of $100TiO_2$@Zn–MnO_2 cell and Zn–MnO_2 cell at 100 mA g^{-1}. c) Self-discharge test $100TiO_2$@Zn–MnO_2 cell and Zn–MnO_2 cell for over 400 h. d) Rate performance of $100TiO_2$@Zn–MnO_2 cell and Zn–MnO_2 cell ranging from 0.1 to 10 A g^{-1}. e) The long term, high rate performance of $100TiO_2$@Zn–MnO_2 cell and Zn–MnO_2 cell at 1 A g^{-1} for 1000 cycles followed by the rate performance.

greatly suppressed. Furthermore, the rate performance is also evaluated at different current densities ranging from 0.1 to 10 A g^{-1} and the corresponding charge–discharge curve at each current density is shown in Figure S12b of the Supporting Information. The $100TiO_2$@Zn-MnO_2 cell shows capacities of 286, 251, 143, 155, 100, and 45 mAh g^{-1}, which is much higher than those of Zn–MnO_2 cell. When the current returns to 1 A g^{-1}, the capacity of $100TiO_2$@Zn-MnO_2 cell returns to 157 mAh g^{-1}, which is still higher than that of Zn–MnO_2 cell (70 mAh g^{-1}). After the rate performance, the long-term high-rate cycling performance at 1 A g^{-1} is evaluated (Figure 4e). It is found that even after 1000 cycles, a capacity of 134 mAh g^{-1} is retained, corresponding to capacity retention of 85%. On the contrary, the capacity of Zn–MnO_2 cell stabilized at 70 mAh g^{-1} and finally failed after 330 cycles. This is also observed in CEs in Figure S13 of the Supporting Information. The CEs

of Zn–MnO_2 cell goes ups and downs at around 97.0% after 180 cycles and reaches the lowest value of 91.2% at the 331st cycle which is consistent with the cycle of cell failure. On the contrary, the CEs of 100TiO_2@Zn are stabilized to be well above 99%, despite the initial activation process. The EIS is also evaluated in Figure S14 of the Supporting Information and both the spectra exhibited a compressed semicircle correlated to the charge transfer resistance (R_{ct}, high frequency), and an inclined line (ω, low frequency). The R_{ct} value decreases after 100 TiO_2 coating, suggesting the enhanced kinetics for Zn ion insertion/extraction.

In conclusion, we demonstrated the application of a thin surface coating of TiO_2 on Zn metal via ALD process. This ultrathin coating of TiO_2 serves as a stable passivation layer for Zn metal, avoiding the direct contact between the zinc plate and electrolyte and suppressing zinc corrosion process and hydrogen evolution, resulting in an enhanced electrochemical performance in both Zn–Zn symmetric cells and Zn–MnO_2 battery. The thickness of protective layer has been further optimized, in which 100 cycles of TiO_2 layer shows the lower corrosion potential. In this way, with the protection of 100 ALD cycles of TiO_2, the undesirable gas evolution is suppressed. The lower gas generation on the outer surface of the zinc plate will maintain the effective contact area between the electrolyte and cathode during cycling, which increases the chance of transport of Zn^{2+} into the bulk of the anode and leads to an improved coulombic efficiency. In this way, the 100TiO_2@Zn anode shows reduced overpotential (72.5 mV) at 1 mA cm^{-2} for over 95 h for Zn–Zn symmetrical battery and additionally, the protection of TiO_2 extended the Zn–MnO_2 cycling performance up to 1000 cycles with the capacity retention of 85% at current density of 3 mA cm^{-2}. Our findings on ALD amorphous TiO_2 layer for the Zn metal anode solidify the case for the implementation of Zn anodes in safe and environmental friendly aqueous Zn-ion systems and pave the way for the continued development of aqueous battery systems.

Experimental Section

Coating Zinc Plate with TiO_2 via ALD: The zinc plates were purchased from Sigma-Aldrich, which were cleaned. Amorphous TiO_2 coating was synthesized in a home-made atomic layer deposition system following reported procedures. Briefly, $TiCl_4$ and H_2O vapors were pulsed into a 120 °C reaction chamber separately with a pulsing time of 0.5 s, separated by 60 s N_2 purging. One deposition cycle involves 0.5 s of H_2O pulse +60 s of N_2 purging +0.5 s of $TiCl_4$ pulse +60 s of N_2 purging. An 8 nm thick TiO_2 coating was deposited by 100 ALD cycles. α-MnO_2 nanowires are prepared via a low-cost, scalable hydrothermal synthesis method using $KMnO_4$ and $MnSO_4$ as reactants.[54]

Structural Characterization: XRD was performed in a Bruker D8 Advance X-ray diffractometer with an area detector, using Cu Kα radiation (λ = 1.5418 Å).). SEM and TEM images were recorded from a JEOL-7100F field-emission SEM, and an FEI TF30 TEM. XPS was obtained from a Thermo Scientific K-alpha XPS instrument with a 400 mm spot size. The flood gun of the XPS instrument was turned on during the measurement.

Electrochemical Characterization: The battery electrodes were fabricated by grounding 70% active material, 20% acetylene black, and 10% poly(tetrauoroethylene) together and then compressed into pellets. The testing batteries were assembled into 2016 coin cells, using a zinc plate as the anode. A solution containing 3 M $Zn(SO_3CF_3)_2$ and 0.1 M $Mn(SO_3CF_3)_2$ was used as the Zn–MnO_2 battery electrolyte. Galvanostatic discharge was studied in a voltage range of 0.8–1.8 V with a multichannel battery testing system (LAND CT 2001A). The mass loading of each electrode was 3 mg cm^{-2}.

Supporting Information

Supporting Information is available from the Wiley Online Library or from the author.

Acknowledgements

K.N.Z. and C.X.W. contributed equally to this work. This work was supported by the National Key Research and Development Program of China (2016YFA0202603), the National Basic Research Program of China (2013CB934103), the Programme of Introducing Talents of Discipline to Universities (B17034), the National Natural Science Foundation of China (51521001 and 51602239), the National Natural Science Fund for Distinguished Young Scholars (51425204), and the Hubei Provincial Natural Science Foundation of China (2016CFB267).

Conflict of Interest

The authors declare no conflict of interest.

Keywords

atomic layer deposition, amorphous TiO_2 layer, zinc anode, zinc ion batteries

Received: June 4, 2018
Revised: July 9, 2018
Published online:

[1] R. Van Noorden, *Nature* **2014**, *507*, 26.
[2] C. P. Grey, J. M. Tarascon, *Nat. Mater.* **2017**, *16*, 45.
[3] Y. Liang, Y. Jing, S. Gheytani, K.-Y. Lee, P. Liu, A. Facchetti, Y. Yao, *Nat. Mater.* **2017**, *16*, 841.
[4] K. Zhao, L. Zhang, R. Xia, Y. Dong, W. Xu, C. Niu, L. He, M. Yan, L. Qu, L. Mai, *Small* **2016**, *12*, 588.
[5] K. Zhao, M. Wen, Y. Dong, L. Zhang, M. Yan, W. Xu, C. Niu, L. Zhou, Q. Wei, W. Ren, X. Wang, L. Mai, *Adv. Energy Mater.* **2017**, *7*, 1601582.
[6] K. Zhao, F. Liu, C. Niu, W. Xu, Y. Dong, L. Zhang, S. Xie, M. Yan, Q. Wei, D. Zhao, L. Mai, *Adv. Sci.* **2015**, *2*, 1500154.
[7] Y. Dong, B. Wang, K. Zhao, Y. Yu, X. Wang, L. Mai, S. Jin, *Nano Lett.* **2017**, *17*, 5740.
[8] D. Kundu, B. D. Adams, V. Duffort, S. H. Vajargah, L. F. Nazar, *Nat. Energy* **2016**, *1*, 16119.
[9] H. Pan, Y. Shao, P. Yan, Y. Cheng, K. S. Han, Z. Nie, C. Wang, J. Yang, X. Li, P. Bhattacharya, K. T. Mueller, J. Liu, *Nat. Energy* **2016**, *1*, 16039.
[10] X. Shan, D. S. Charles, Y. Lei, R. Qiao, G. Wang, W. Yang, M. Feygenson, D. Su, X. Teng, *Nat. Commun.* **2016**, *7*, 13370.
[11] J. Yan, J. Wang, H. Liu, Z. Bakenov, D. Gosselink, P. Chen, *J. Power Sources* **2012**, *216*, 222.
[12] J. O. G. Posada, A. J. R. Rennie, S. P. Villar, V. L. Martins, J. Marinaccio, A. Barnes, C. F. Glover, D. A. Worsley, P. J. Hall, *Renewable Sustainable Energy Rev.* **2017**, *68*, 1174.

[13] J. Liu, C. Xu, Z. Chen, S. Ni, Z. X. Shen, *Green Energy Environ.* **2017**, *3*, 20.
[14] X. Dong, L. Chen, X. Su, Y. Wang, Y. Xia, *Angew. Chem., Int. Ed.* **2016**, *55*, 7474.
[15] C. Yang, X. Ji, X. Fan, T. Gao, L. Suo, F. Wang, W. Sun, J. Chen, L. Chen, F. Han, L. Miao, K. Xu, K. Gerasopoulos, C. Wang, *Adv. Mater.* **2017**, *29*, 1701972.
[16] A. M. Zamarayeva, A. E. Ostfeld, M. Wang, J. K. Duey, I. Deckman, B. P. Lechêne, G. Davies, D. A. Steingart, A. C. Arias, *Sci. Adv.* **2017**, *3*, e1602051.
[17] C. Yan, X. Wang, M. Cui, J. Wang, W. Kang, C. Y. Foo, P. S. Lee, *Adv. Energy Mater.* **2014**, *4*, 1301396.
[18] J. F. Parker, C. N. Chervin, E. S. Nelson, D. R. Rolison, J. W. Long, *Energy Environ. Sci.* **2014**, *7*, 1117.
[19] X. Wang, F. Wang, L. Wang, M. Li, Y. Wang, B. Chen, Y. Zhu, L. Fu, L. Zha, L. Zhang, Y. Wu, W. Huang, *Adv. Mater.* **2016**, *28*, 4904.
[20] Y. Zeng, X. Zhang, Y. Meng, M. Yu, J. Yi, Y. Wu, X. Lu, Y. Tong, *Adv. Mater.* **2017**, *29*, 1700274.
[21] S. Islam, M. H. Alfaruqi, V. Mathew, J. Song, S. Kim, S. Kim, J. Jo, J. P. Baboo, D. T. Pham, D. Y. Putro, Y.-K. Sun, J. Kim, *J. Mater. Chem. A* **2017**, *5*, 23299.
[22] G. G. Yadav, X. Wei, J. Huang, J. W. Gallaway, D. E. Turney, M. Nyce, J. Secor, S. Banerjee, *J. Mater. Chem. A* **2017**, *5*, 15845.
[23] W. Sun, F. Wang, S. Hou, C. Yang, X. Fan, Z. Ma, T. Gao, F. Han, R. Hu, M. Zhu, C. Wang, *J. Am. Chem. Soc.* **2017**, *139*, 9775.
[24] N. Zhang, F. Cheng, Y. Liu, Q. Zhao, K. Lei, C. Chen, X. Liu, J. Chen, *J. Am. Chem. Soc.* **2016**, *138*, 12894.
[25] B. Li, J. Quan, A. Loh, J. Chai, Y. Chen, C. Tan, X. Ge, T. S. A. Hor, Z. Liu, H. Zhang, Y. Zong, *Nano Lett.* **2017**, *17*, 156.
[26] G. G. Yadav, J. W. Gallaway, D. E. Turney, M. Nyce, J. Huang, X. Wei, S. Banerjee, *Nat. Commun.* **2017**, *8*, 14424.
[27] P. He, M. Yan, G. Zhang, R. Sun, L. Chen, Q. An, L. Mai, *Adv. Energy Mater.* **2017**, *7*, 1601920.
[28] W. Liu, J. Hao, C. Xu, J. Mou, L. Dong, F. Jiang, Z. Kang, J. Wu, B. Jiang, F. Kang, *Chem. Commun.* **2017**, *53*, 6872.
[29] W. Xu, S. Dai, G. Liu, Y. Xi, C. Hu, X. Wang, *Electrochim. Acta* **2016**, *203*, 1.
[30] W. Xu, Z. Jiang, Q. Yang, W. Huo, M. S. Javed, Y. Li, L. Huang, X. Gu, C. Hu, *Nano Energy* **2018**, *43*, 168.
[31] M. H. Alfaruqi, V. Mathew, J. Gim, S. Kim, J. Song, J. P. Baboo, S. H. Choi, J. Kim, *Chem. Mater.* **2015**, *27*, 3609.
[32] S.-D. Han, S. Kim, D. Li, V. Petkov, H. D. Yoo, P. J. Phillips, H. Wang, J. J. Kim, K. L. More, B. Key, R. F. Klie, J. Cabana, V. R. Stamenkovic, T. T. Fister, N. M. Markovic, A. K. Burrell, S. Tepavcevic, J. T. Vaughey, *Chem. Mater.* **2017**, *29*, 4874.
[33] B. J. Hertzberg, A. Huang, A. Hsieh, M. Chamoun, G. Davies, J. K. Seo, Z. Zhong, M. Croft, C. Erdonmez, Y. S. Meng, D. Steingart, *Chem. Mater.* **2016**, *28*, 4536.
[34] L. Zhang, L. Chen, X. Zhou, Z. Liu, *Adv. Energy Mater.* **2015**, *5*, 1400930.
[35] C. Xia, J. Guo, P. Li, X. Zhang, H. N. Alshareef, *Angew. Chem., Int. Ed.* **2018**, *57*, 3943.
[36] S. Yasuji, *Physica* **1986**, *140A*, 134.
[37] J. F. Parker, C. N. Chervin, I. R. Pala, M. Machler, M. F. Burz, J. W. Long, D. R. Rolison, *Science* **2017**, *356*, 415.
[38] T. K. A. Hoang, T. N. L. Doan, K. E. K. Sun, P. Chen, *RSC Adv.* **2015**, *5*, 41677.
[39] J. L. Yang, Y. F. Yuan, H. M. Wu, Y. Li, Y. B. Chen, S. Y. Guo, *Electrochim. Acta* **2010**, *55*, 7050.
[40] L.-P. Wang, N.-W. Li, T.-S. Wang, Y.-X. Yin, Y.-G. Guo, C.-R. Wang, *Electrochim. Acta* **2017**, *244*, 172.
[41] H. Li, C. Han, Y. Huang, Y. Huang, M. Zhu, Z. Pei, Q. Xue, Z. Wang, Z. Liu, Z. Tang, Y. Wang, F. Kang, B. Li, C. Zhi, *Energy Environ. Sci.* **2018**, *11*, 941.
[42] S. Higashi, S. W. Lee, J. S. Lee, K. Takechi, Y. Cui, *Nat. Commun.* **2016**, *7*, 11801.
[43] A. R. Mainar, L. C. Colmenares, J. A. Blázquez, I. Urdampilleta, *Int. J. Energy Res.* **2017**, *42*, 903.
[44] G. Garcia, E. Ventosa, W. Schuhmann, *ACS Appl. Mater. Interfaces* **2017**, *9*, 18691.
[45] M. Chamoun, B. J. Hertzberg, T. Gupta, D. Davies, S. Bhadra, B. Van Tassell, C. Erdonmez, D. A. Steingart, *NPG Asia Mater.* **2015**, *7*, e178.
[46] J. F. Parker, E. S. Nelson, M. D. Wattendorf, C. N. Chervin, J. W. Long, D. R. Rolison, *ACS Appl. Mater. Interfaces* **2014**, *6*, 19471.
[47] K. E. K. Sun, T. K. A. Hoang, T. N. L. Doan, Y. Yu, X. Zhu, Y. Tian, P. Chen, *ACS Appl. Mater. Interfaces* **2017**, *9*, 9681.
[48] W. Luo, C.-F. Lin, O. Zhao, M. Noked, Y. Zhang, G. W. Rubloff, L. Hu, *Adv. Energy Mater.* **2017**, *7*, 1601526.
[49] Y. Zhao, L. V. Goncharova, A. Lushington, Q. Sun, H. Yadegari, B. Wang, W. Xiao, R. Li, X. Sun, *Adv. Mater.* **2017**, *29*, 1606663.
[50] A. C. Bronneberg, C. Höhn, R. van de Krol, *J. Phys. Chem. C* **2017**, *121*, 5531.
[51] N. Zhang, F. Cheng, J. Liu, L. Wang, X. Long, X. Liu, F. Li, J. Chen, *Nat. Commun.* **2017**, *8*, 405.
[52] H. Wang, M. Wang, Y. Tang, *Energy Storage Mater.* **2018**, *13*, 1.
[53] L. Dong, X. Ma, Y. Li, L. Zhao, W. Liu, J. Cheng, C. Xu, B. Li, Q.-H. Yang, F. Kang, *Energy Storage Mater.* **2018**, *13*, 96.
[54] B. Wu, G. Zhang, M. Yan, T. Xiong, P. He, L. He, X. Xu, L. Mai, *Small* **2018**, *14*, 1703850.

